Multi-tuned Narrowband Damping for Suppressing MMC High-Frequency Oscillations

Pengxiang Huang, *Student Member, IEEE*, and Luigi Vanfretti, *Senior Member, IEEE*

***Abstract*—Modular multilevel converters have been widely reported to experience high-frequency oscillations with the power system to which they are connected in HVdc applications, and the root cause is that the system resonance frequencies fall into the delay-induced non-passive region of the MMCs. This paper presents a multi-tuned narrowband damping control scheme to selectively and narrowly enhance the passivity of an MMC around multiple resonance frequencies, and thereby damp the associated high-frequencies oscillations. First, this paper presents a detailed process for simplifying the complete matrix-based impedance model of MMC into a high-frequency impedance model suitable for damping design. Second, using the simplified model, the effect and comprehensive design of the proposed multi-tuned damping controller are described from a virtual admittance perspective, making it possible to simultaneously damp the MMC impedance around multiple resonance frequencies in the high-frequency range. The proposed design method carefully takes into account the coupling effect among multiple damping controllers targeting oscillations at different frequencies, in order to avoid potential unintended interferences. The performance of the proposed narrowband damping method is verified in EMT simulations by implementing it to suppress high-frequency oscillations in three different MMC-based applications.**

***Index Terms*—MMC, impedance-based stability, high-frequency oscillations, narrowband damping, virtual admittance, active damping**

I. Introduction

A. Motivation

HIGH frequency oscillation (HFO) events have been widely reported in modular multilevel converter (MMC)-based HVdc applications [1]–[4], and are attributed to the negative damping of the MMC impedance at the system resonance frequency. The root cause of the negative damping of MMC is mainly due to the phase lag in the MMC impedance introduced by the time delay, including digital control delay and modulation sampling and hold delay. Such HFOs can appear at any frequency from a few hundred Hz to the Nyquist frequency, and may exist at more than one frequency at a time [5], which presents challenges for designing damping methods. In addition, the ac system impedance can also exhibit non-passive behavior at high frequencies when it contains power converters with active control functions [5] (e.g., turbine converters and STATCOMs). According to the impedance-based stability criterion [6], an oscillation may also be formed between the MMC and the ac system if the net damping is negative at the system resonance frequency (i.e., phase difference of impedance between the MMC and the ac system is larger than 180°), even if the MMC has no negative damping at that frequency. Therefore, it is necessary to develop a damping approach that is capable of introducing additional positive damping at the specific frequency instead of only eliminating the negative damping of the MMC (i.e., only making real part of the converter impedance be 0). This motivation is a significant part of the work presented in this paper.

B. Literature Review

Impedance-based small-signal stability analysis has been recognized as an effective approach for studying HFOs between MMC and the ac system [1], [3]. In order to develop a solution to counteract the oscillation issues of MMC, several small-signal impedance modeling methods of MMC have been proposed in recent years, e.g. multi-harmonic linearization method [7], [8] and harmonic state-space method [9], [10]. However, because the internal dynamics of the MMC and frequency coupling are taken into account in the development of these methods, the resulting MMC impedance is represented in a high-order matrix form. This can make it challenging to design damping control schemes as the impedance model of the MMC is not straightforward to handle. Therefore, considering that internal dynamics and coupling over frequency can be ignored in the high-frequency range [11], most previous studies in the literature have adopted a high-frequency impedance model in a single transfer function form, which is suitable for designing damping controls [3]–[5], [12]. However, the high-frequency impedance models employed in these studies share a common limitation with respect to the MMC control modes considered, as they can only represent grid-following MMCs in dc voltage control with a unity power factor and grid-forming MMCs in fixed ac voltage and frequency control. In addition, the derivation of the high-frequency impedance model is not adequately elucidated in the literature, and the rationale for neglecting the internal dynamics of MMC and certain controllers remains unidentified, which needs to be clarified.

In general, suppressing HFOs of MMC can be achieved through passive damping methods and active damping methods. Passive damping [13], [14] can be applied to damp the resonance over a broad frequency range, but may come with additional costs, power losses, and installation space requirements. In contrast, active damping methods can be more cost effective when used in mitigating HFOs. In the literature, active damping methods can be broadly divided into three categories: (i) modifying the parameters of existing controls; (ii) inserting lowpass filtering functions into existing controls; or (iii) adding additional control functions supplementary for damping. Modifying the controller parameters is an effective

solution to mitigate HFO below the cutoff frequency of the controller, normally below a few hundred Hz. However, this approach can have a significant impact on the transient performance of MMC. Cascading a lowpass filter with the controllers to remove the undesirable signal component associated with oscillation is relatively straightforward [3], [4]. The downside of this method is the phase shift introduced by the lowpass filtering function, especially with heavy filtering, which usually leads to more negative damping of the MMC at the passband frequency of the filter, thereby causing the MMC to be more prone to stability issues at that frequency range. In addition, an inappropriate selection of the filter's bandwidth and order can potentially lead to degradation of controller's performance and even instability. Incorporating an additional damping controller to reshape the converter impedance is another option to mitigate the oscillation, and the techniques developed to achieve this include broadband and narrowband damping. A major challenge of this approach is that the additional damping function itself is also subjected to the impact of time delay [15], particularly in broadband damping, because the phase shift introduced by the delay can be difficult to compensate for over a wide frequency range. While it might be possible to compensate for this phase shift within a certain intended frequency range [16], doing so usually causes more negative damping at nearby frequencies [5]. Furthermore, the design of the broadband damping can interfere with existing control functions, deteriorating the overall stability of the system at unintended frequencies. To minimize any negative effects of the damping function at unintended frequencies, a bandpass filter can be used to limit the damping function to a specified range, which leads to the narrowband damping method.

Reference [17] demonstrates such a method by using a biquadratic filter to improve the phase margin of the two-level voltage source converter (2L-VSC) in the near-synchronous range. The time-delay compensation, however, is not taken into account since the delay effect is approximately unity in that frequency range. Reference [18], [19] presented a similar damping method based on the complex bandpass filter but using a phase-lead unit to compensate for the phase shift caused by time delay. However, additional phase shift on the narrowband damping function, which are posed by the control loops, are not considered. Note that all the three works are built on the ac current feedforward loop, and the damping effect can be viewed as a virtual impedance in series with the converter [20]. In [5], it is demonstrated that voltage feedforward-based narrowband damping can achieve virtually the same damping effect as the current feedforward-based method used in [17]–[19], but introduces less negative damping outside the intended damping range (see Fig. 3 in [5]). As a result, the voltage feedforward-based damping is considered more desirable for suppressing HFOs of MMC. However, it has been observed that existing narrowband damping methods for resolving the HFO issue focus on only one specific intended frequency. In other words, these methods cannot be used to mitigate multiple oscillations and cannot be applied to a wide frequency range.

This paper presents a methodology to derive simplified high-frequency impedance models of MMCs, starting from a complete matrix-based impedance expression (modeled by multi-harmonic linearization method), in which five typical control schemes for MMC in the HVdc application are considered. The process is divided into three steps and provides a clear explanation of why internal dynamics, dc voltage control, phase-locked loop, and circulating current control can be neglected in the high-frequency range. With the derived high-frequency impedance model, a multi-tuned narrowband damping method is proposed to suppress multiple high-frequency oscillations issue. To fully compensate for the phase lag in the damping function caused by time delay, control loop and plant transfer functions at intended resonance frequencies, the damping function is combined with a phase-lead function, and the design of the phase-lead function is thoroughly explained. In addition, a systematic design procedure is presented to allow for the simultaneous design of multiple damping functions, preventing unintended effects due to mutual coupling among them. It is noteworthy that the narrowband damping necessitates an online resonance detection block to provide resonance frequencies for damping control design, in order to address changes in resonance frequencies due to variation in grid configuration, altering control modes and changing operating conditions. The algorithms for identifying the resonance frequencies and activating damping controls in the online resonance detection block are detailed in [21]–[23]; however, to limit the scope of the paper, they will not be discussed further.

C. Contributions

The specific contributions of this paper are the following:

- Presenting a comprehensive method to simplify the complete high-order matrix-based impedance model of MMC obtained by multi-harmonic linearization method into the high-frequency impedance model suitable for control design, in which different control modes of MMC can be captured.
- Proposing a multi-tuned narrowband damping method to improve the passivity of a MMC around multiple intended frequencies simultaneously. Additionally, investigating and elaborating on the mutual coupling effects that arise when multiple narrowband damping controllers are used.
- Proposing a design procedure for multiple narrowband damping controllers with compensation for mutual-coupling effects.

D. Organization

The rest of the paper is organized as follows. Section II describes a typical structure for an MMC-based system and derives the high-frequency impedance model of MMC that can be used for stability analysis and damping control design at high frequencies. Based on the derived high-frequency impedance model, the effect of the proposed voltage feedforward control on MMC is discussed from a paralleled virtual admittance perspective in Section III, along with a discussion of phase lags that the designed damping function is subjected to and how to compensate for them. Section IV provides a

virtual admittance-based method to design single- or multi-tuned damping controls to enhance the passivity of MMC around single or multiple frequencies. By performing simulations in different MMC-based systems, Section V validates the effectiveness of the proposed damping control method in three typical MMC-based application scenarios. Section VI concludes this paper.

II. MMC and High-frequency Impedance Model

A. MMC and Control Structures

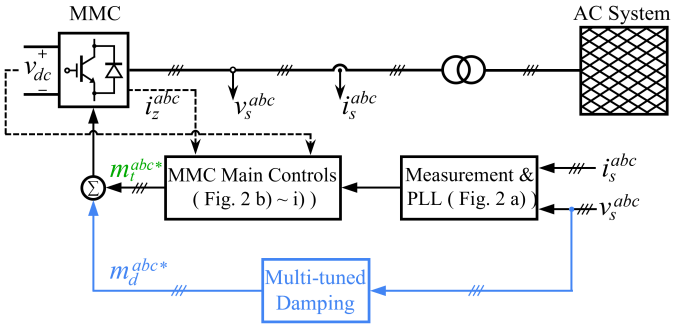

Fig. 1. Schematic of the MMC-based system under study and its control structure.

Fig. 1 shows a single-line diagram of a MMC-based system, which also indicates where MMC main controllers and the proposed multi-tuned narrowband damping controller should be introduced. The ac system can consist either passive elements only, such as overhead transmission line, cables, and passive filters, or active elements involving power converters (e.g., Type-IV wind turbine). When the MMC operates in grid-following mode, its primary objective is to regulate the output ac current. Thus, it is referred to as an ac current controlled MMC (ACC-MMC) in this work. On the other hand, when the MMC is operated in grid-forming mode (or islanded mode for wind integration), the output ac voltage and its frequency are actively controlled by the MMC. Therefore, this type of MMC is denoted as an ac voltage controlled MMC (AVC-MMC) for the sake of simplicity.

For MMC-based HVdc applications, MMC control modes typically include dc-bus voltage control, active/reactive power control (denoted as "P & Q" mode) and ac voltage control with fixed amplitude and frequency (referred to as "fixed V_{ac} & f"). The dc-bus voltage control mode can be further divided into two types, namely, with and without reactive power regulation [24]. In this paper, the MMC in the dc-bus voltage controlled mode with unity power factor is marked as "V_{dc} & $Q=0$", while the dc-bus voltage controlled mode with reactive power regulation is denoted as "V_{dc} & Q". In addition, for MMCs equipped with the fixed V_{ac} & f mode, an inner ac current controller may or may not be used, depending on stability considerations [10], [12], [25]. In this work, when the inner ac current control is not used, the control mode is denoted as "single-loop fixed V_{ac} & f"; meanwhile when the inner ac current control is used, the control mode is referred to as "dual-loop fixed V_{ac} & f". The block diagram of different control schemes for ACC-MMC and AVC-MMC are depicted in Fig. 2.

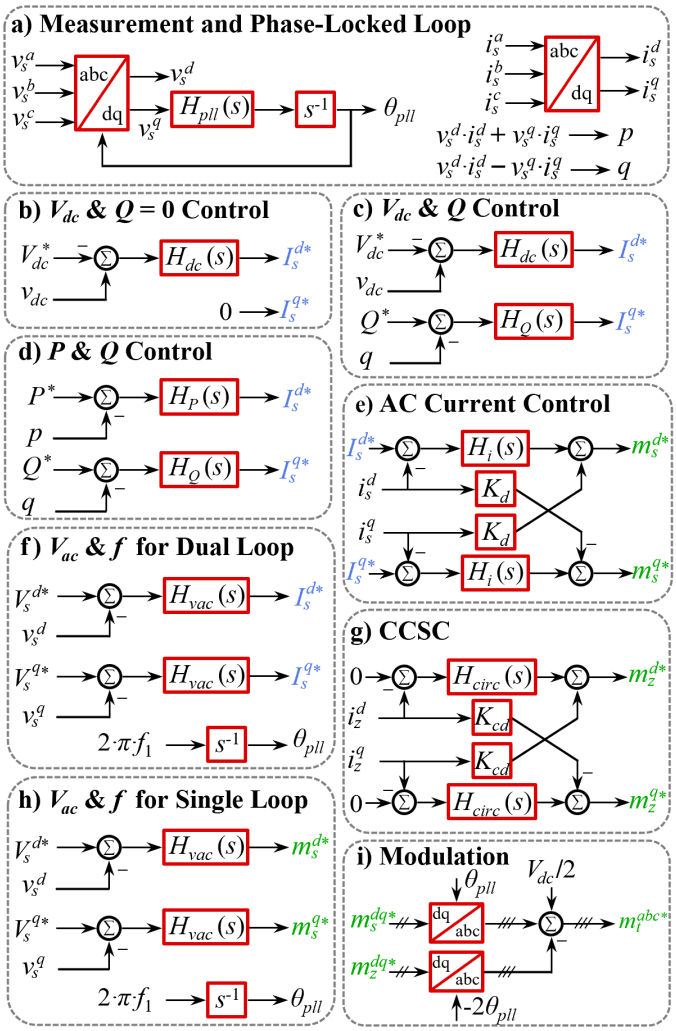

Fig. 2. Block diagram of the main control schemes for MMC.

B. Steps to Derive High-frequency Impedance Model of MMC

Although the complete matrix-based impedance model can well represent both internal and external dynamics of MMC, such high-order matrix form makes designing damping controls more complex and computationally demanding, particularly when used to design multi-tuned narrowband damping controllers. Therefore, this subsection aims to propose a method to simplify the complete matrix-based impedance model of MMC, which is modeled by the multi-harmonic linearization method, into a high-frequency impedance model represented by a single transfer function.

According to [8], the detailed small-signal model of MMC's ac-side impedance can be expressed by

$$\mathbf{Y}_{ac} = (\mathbf{U}-\mathbf{K})\mathbf{A}_i^{-1}\mathbf{A}_v \tag{1}$$

$$\begin{cases} \mathbf{A}_i = \mathbf{U} + \mathbf{Y}_l[\mathbf{M}_u\mathbf{Z}_c\mathbf{M}_u + (\mathbf{V}_u + \mathbf{M}_u\mathbf{Z}_c\mathbf{I}_u)\mathbf{Q}_i\mathbf{D}] \\ \mathbf{A}_v = \mathbf{Y}_l[\mathbf{U} + (\mathbf{V}_u + \mathbf{M}_u\mathbf{Z}_c\mathbf{I}_u)\mathbf{P}_v\mathbf{D}] \\ \begin{cases} \mathbf{U} = \mathbf{diag}[(1,\ldots,1)]_{n\times n} \\ \mathbf{K} = \mathbf{diag}[(-1)^{S_k}]_{n\times n} \end{cases}; \quad S_k = \begin{cases} 1 & \text{if} \quad k = 2i \\ 0 & \text{if} \quad k = 2i-1 \end{cases} \end{cases} \tag{2}$$

where n is the selected harmonic truncation order for multi-harmonic linearization method, which is typically 7; $i = 0, \pm1, \pm2, \cdots$. The expression of the ac-side admittance of the MMC is the center element of matrix $\mathbf{Y}_{ac}$. The matrix $\mathbf{Y}_l$, $\mathbf{Z}_c$, are diagonal matrices representing the arm impedance and the impedance of the equivalent module capacitor per arm, respectively. $\mathbf{V}_u$, $\mathbf{I}_u$, $\mathbf{M}_u$ in the Toeplitz matrix form, describes the steady-state signals of the sum capacitor voltage per arm, arm current and modulation index, respectively. The matrix $\mathbf{Q}_i$ represents the effect resulting from arm current perturbations on the modulation index via current-related controllers. The matrix $\mathbf{P}_v$ represents the effect resulting from arm voltage perturbations on the modulation index through voltage-related controllers. The matrix $\mathbf{D}$ represents the time delay effect. For more details on how to model $\mathbf{Q}_i$ and $\mathbf{P}_v$ for different control schemes, and how to express the non-zero elements in the two matrices, please refer to [8], [26]. In the sequel, the proposed method to simplify this matrix-based impedance model is described in three sequential steps.

1) **1st**-*step Simplification*

Note that, the elements of matrix $\mathbf{Z}_c$ represent the impedance of equivalent module capacitors per arm, whose elements are virtually zero in the high-frequency range. As a result, the matrix $\mathbf{Z}_c$ reduces to a null matrix, allowing for further simplification of (2), resulting in

$$\begin{cases} \mathbf{A}_i = \mathbf{U} + \mathbf{Y}_l \mathbf{V}_u \mathbf{Q}_i \mathbf{D} \\ \mathbf{A}_v = \mathbf{Y}_l (\mathbf{U} + \mathbf{V}_u \mathbf{P}_v \mathbf{D}) \end{cases}. \tag{3}$$

This simplification step suggests that any small-signal responses arising from the interaction between small-signal perturbations and SMs' capacitors can be disregarded in the high-frequency range. As of now, $\mathbf{Q}_i$ and $\mathbf{P}_v$ can only affect $\mathbf{A}_i$ and $\mathbf{A}_v$ through their multiplication with $\mathbf{V}_u$ and $\mathbf{Y}_l$. Subsequent simplification steps take into account the control scheme employed in the MMC.

2) **2nd**-*step Simplification*

In general, for MMCs in HVdc applications, $\mathbf{Q}_i$ and $\mathbf{P}_v$ can be expressed as [8]

$$\begin{cases} \mathbf{Q}_i = \mathbf{G}_i + \mathbf{G}_{circ} + \mathbf{G}_{ir}(\mathbf{G}_Q \mathbf{V_Q} + \mathbf{G}_P \mathbf{V_P} - \mathbf{G}_{v_{dc}} \mathbf{Z}_{dc}) \\ \mathbf{P}_v = \mathbf{G}_{ff} + \mathbf{G}_{pll} + \mathbf{G}_{ir}(\mathbf{G}_{v_{ac}} + \mathbf{G}_Q \mathbf{I_Q} + \mathbf{G}_P \mathbf{I_P}) \end{cases} \tag{4}$$

where, $\mathbf{G}_i$, $\mathbf{G}_{circ}$, $\mathbf{G}_P$, $\mathbf{G}_Q$, $\mathbf{G}_{v_{dc}}$, $\mathbf{G}_{v_{ac}}$, $\mathbf{G}_{pll}$, $\mathbf{G}_{ff}$ represent the control gain matrix of ac current control, circulating current suppressing control (CCSC), active power control, reactive power control, dc-bus voltage control, ac voltage control, phase-locked loop (PLL) and grid voltage feedforward. $\mathbf{G}_{ir}$ represents the ac current loop effect on the small-signal perturbation on the reference values of current control; while $\mathbf{V_P}$, $\mathbf{V_Q}$, $\mathbf{I_P}$ and $\mathbf{I_Q}$ describe the steady state values of the ac voltage and ac current in dq-axis, respectively. Readers can refer to [8] for more detailed expressions of each of the matrices mentioned above. It is worth mentioning that, depending on the specific control scheme in use in the MMC, certain matrices on the right-hand side of (4) might be zero when the controllers represented by these matrices are not used.

Observe that the small-signal perturbation on the dc-side $\hat{\mathbf{v}}_{\mathbf{dc}}$ relies on the interaction between arm current perturbations $\hat{\mathbf{i}}_u$ with the SMs' capacitor dynamics, i.e. $v = \frac{1}{C}\int i dt$. Due to the low-pass characteristic of the integral dynamics, the high-frequency components in $\hat{\mathbf{i}}_u$ will experience attenuation from the SMs' capacitors. Thus, $\mathbf{G}_{v_{dc}}$ can then be reduced to zero when analyzing the MMC impedance at high frequencies. In addition, referring back to (3) and (4), it can be observed that $\mathbf{G}_{circ}$ has virtually no effect on $\mathbf{A}_i$ in the high-frequency range, owing to two reasons: 1) upper arm voltage perturbation $\hat{\mathbf{v}}_u$ will be attenuated by $\mathbf{Y}_l$ at f_p & $f_p \pm f_1$, along with the attenuation by $\mathbf{Z}_c$ at $f_p \pm f_1$; 2) the effect of $\mathbf{G}_{circ}$ is only on the circulating component in the arm current $\hat{\mathbf{i}}_u$ (i.e., common-mode current) and $\mathbf{G}_{circ}$ can only affect the MMC ac-side impedance through its coupling with $\mathbf{V}_u$ that includes harmonics solely below the 3^{rd}-order. Consequently, the multiplication between $\mathbf{V}_u$ and $\mathbf{G}_{circ}$ results in a negligible effect in the high-frequency range, indicating $\mathbf{G}_{circ}$ can be replaced by a null-matrix. This simplification leads to two important outcomes: 1) in the high-frequency range, dc-side small-signal responses propagated from the ac-side can be ignored, as also noted in [14]; and 2) the circulating current control has negligible effect on the MMC's high-frequency impedance.

3) **3rd**-*step Simplification*

After replacing matrix $\mathbf{G}_{v_{dc}}$ and $\mathbf{G}_{circ}$ in (4) by a null-matrix, the remaining matrix in (4) represents the controllers whose input contains only the ac-side current or voltage. As explained in [7], each non-zero element of $\mathbf{G}_{pll}$ includes a transfer function representing the closed-loop response of the PLL, that is, $1/[1+\sqrt{\frac{3}{2}}V_1\frac{H_\theta(s)}{s}]$, where V_1 is the fundamental RMS voltage of the MMC and $H_\theta(s)$ represents the PI compensator of the PLL. Considering the low bandwidth of the PLL and 2^{nd}-order lowpass nature of $1/[1+\sqrt{\frac{3}{2}}V_1\frac{H_\theta(s)}{s}]$, the high-frequency components in the input of the PLL will be attenuated by the PLL itself, and thus, cannot affect the MMC impedance at high frequencies. Consequently, $\mathbf{G}_{pll}$ can also be reduced to a null matrix. This simplification step indicates that the PLL has no effect on the MMC impedance in the high-frequency range.

Based on the aforementioned three-step simplification process, (4) can be simplified to the following:

$$\begin{cases} \mathbf{Q}_i = \mathbf{G}_i + \mathbf{G}_{ir}(\mathbf{G}_Q \mathbf{V_Q} + \mathbf{G}_P \mathbf{V_P}) \\ \mathbf{P}_v = \mathbf{G}_{ff} + \mathbf{G}_{ir}(\mathbf{G}_{v_{ac}} + \mathbf{G}_Q \mathbf{I_Q} + \mathbf{G}_P \mathbf{I_P}) \end{cases}. \tag{5}$$

Combining (1), (2) and (5), then extracting the center element of this combined matrix, the resulting simplified high-frequency impedance of MMC is given as the reciprocal of the center element. For the sake of conciseness, the high-frequency MMC impedance model with different control schemes are summarized in Table I, in which: 1) $G_i(s) = H_i(s - j\omega_1) - jK_d$ represents the ac current controller in the dq-reference frame, where $H_i(s)$ designates the PI compensator for ac current control, and $K_d = j\omega_1 L_{eq}$ is the dq current decoupling gain; 2) $G_{ff}(s) = -F^v_{filter}(s)$ represents a grid voltage feed-forward loop with low pass filter (see [2], [27]), typically having

TABLE I
SIMPLIFIED MMC HIGH-FREQUENCY IMPEDANCE MODEL IN DIFFERENT CONTROL MODES.

Control Modes	**Null Matrix in** (5)	**High-frequency Impedance of MMC**
V_{dc} & $Q=0$	$\mathbf{G}_P$, $\mathbf{G}_Q$, $\mathbf{G}_{v_{ac}}$	$\frac{R_{eq}+sL_{eq}+e^{-sT_d}G_i(s)}{1+e^{-sT_d}G_{ff}(s)}$
V_{dc} & Q	$\mathbf{G}_P$, $\mathbf{G}_{v_{ac}}$	$\frac{R_{eq}+sL_{eq}+e^{-sT_d}[G_i(s)+\frac{3}{4}G_i(s)G_Q(s)V_d]}{1+e^{-sT_d}[-\frac{3}{4}G_i(s)G_Q(s)(I_d+jI_q)+G_{ff}(s)]}$
P & Q	$\mathbf{G}_{v_{ac}}$	$\frac{R_{eq}+sL_{eq}+e^{-sT_d}[G_i(s)+\frac{3}{2}G_i(s)G_P(s)V_d]}{1+e^{-sT_d}G_{ff}(s)}$
fixed V_{ac} & f (single-loop)	$\mathbf{G}_P$, $\mathbf{G}_Q$, $\mathbf{G}_i$ ($\mathbf{G}_{ir}=1$)	$\frac{R_{eq}+sL_{eq}}{1+e^{-sT_d}G_{v_{ac}}(s)}$
fixed V_{ac} & f (dual-loop)	$\mathbf{G}_P$, $\mathbf{G}_Q$,$\mathbf{G}_{ff}$	$\frac{R_{eq}+sL_{eq}+e^{-sT_d}G_i(s)}{1+e^{-sT_d}G_{v_{ac}}(s)G_{ir}(s)}$

low bandwidth, thus $G_{ff}(s)$ can be neglected when analyzing MMC high-frequency characteristics as described in [11], [19]; 3) $G_{ir}(s)=H_i(s-j\omega_1)$ represents the ac current control effects on the current reference generated by an outer control loop[1]; 4) $G_{v_{ac}}(s)=H_v(s-j\omega_1)$ represents the ac voltage controller in the dq-reference frame, where $H_v(s)$ designates the PI compensator for the ac voltage regulator; 5) $G_{P(Q)}(s)=H_{P(Q)}(s-j\omega_1)$ represents the active (reactive) power controller in the dq-reference frame, where $H_{P(Q)}(s)$ represents a PI compensator for the active (reactive) power regulator.

TABLE II
ELECTRICAL PARAMETERS FOR ACC-MMC AND AVC-MMC

Parameter	**Symbol**	**Value**	**Unit**
rated active power	P_N	900	MW
rated ac side voltage	U_N	300	kV RMS ph-ph
rated dc side voltage	V_{dc}	$\pm$320	kV
arm reactor impedance	R_s+jL_s	$0.1+j0.05$	Ω
submodules per arm	N_{sm}	200	N/A
submodule capacitance	C_{sm}	4.66	mF
time delay	e^{-sT_d}	200	μs

TABLE III
CONTROL SPECIFICATIONS FOR ACC-MMC AND AVC-MMC

Control Mode	K_p	K_i	K_d
dc voltage control	0.0065	0.2	NA
ac current control	22.2	27915.5	7.85
circulating current control	22.2	13957.7	31.42
active/reactive power control	1.5	300	N/A
phase-locked loop	1.48×10^{-4}	0.0093	N/A
ac voltage control	0.5	54.4	N/A

To validate the above discussion on simplifying MMC impedance model, the derived high-frequency impedance model of MMC are verified by its comparison with numerical scan of the impedance of the MMC defined in Table II. This comparison is illustrated in Fig. 3 and Fig. 4. The controller

[1]Note that, if the inner current control is not used, $G_{ir}(s)=1$.

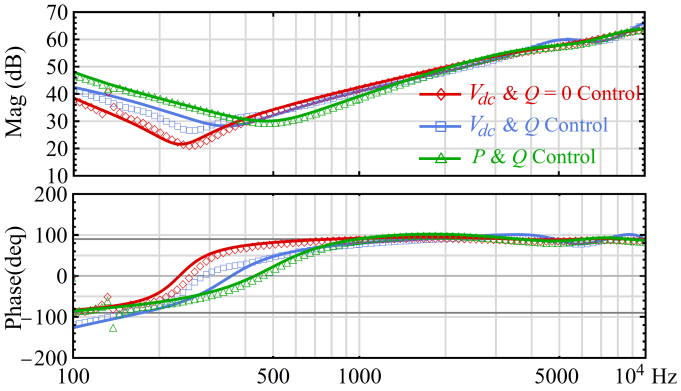

Fig. 3. Comparison of analytical simplified high-frequency impedance model (solid lines) and numerical scan of ACC-MMCs (markers)

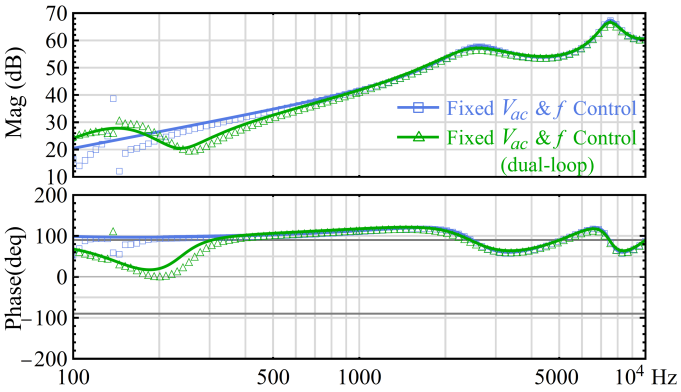

Fig. 4. Comparison of analytical simplified high-frequency impedance model (solid lines) and numerical scan of AVC-MMCs (markers)

specifications for both ACC-MMC and AVC-MMC are listed in Table III. As can be observed from the comparisons, the high-frequency ACC-MMC impedance models are accurate for frequencies above ~300 to 400 Hz, while the high-frequency AVC-MMC impedance models are accurate for frequencies above ~200 Hz. In addition, the power control loop of ACC-MMC (i.e., V_{dc} & Q and P & Q control modes) and the inner current loop of AVC-MMC have the effect of raising the starting frequency of the negative damping region of MMC, which makes the MMC less likely to develop

oscillations with the ac system in the medium frequency range (100Hz to 1000Hz). On the other hand, for the frequency range above 1000 Hz, the AVC-MMC impedance responses are nearly the same as the inner current loop has virtually no effect on the AVC-MMC impedance above ~800 Hz.

C. General Form for Damping Control Design

Considering the impedance model of MMC in different control schemes presented in Table I, the simplified model can be expressed in a general form for the ease of damping control design, which is given by

$$Z_p(s) = \frac{R_{eq} + sL_{eq} + e^{-sT_d}G_c(s)}{1 + e^{-sT_d}G_v(s)} = \frac{N_p(s)}{D_p(s)} = \frac{1}{Y_p(s)} \tag{6}$$

where $N_p(s)$ and $D_p(s)$ represent the numerator and denominator of $Z_p(s)$ respectively. $G_c(s)$ and $G_v(s)$ come in different form as shown in Table I.

In order to demonstrate the generality of the proposed damping design method, this paper will use MMCs with three different control schemes as the examples: 1) ACC-MMC in V_{dc} & $Q = 0$ mode; ACC-MMC in P & Q mode; 3) AVC-MMC in single-loop fixed V_{ac} & f mode.

III. Narrowband Damping of MMC

A. Impedance-based Stability Analysis of HF Oscillations

Fig. 5 a) depicts the equivalent circuit of an ACC-MMC connected to a grid and Fig. 5 b) displays the equivalent circuit of an AVC-MMC connected by a wind farm, where $Z_p(s)$ represents the high-frequency MMC impedance developed in Section II, $Z_g(s)$ and $Z_{WF}(s)$ represent the ac grid impedance and wind farm impedance, respectively. Stable operation of the ACC-MMC in circuit a) requires that the output current of the MMC (indicated as $I_{PCC}(s)$) be stable. On the other hand, for a stable operation of the AVC-MMC in circuit b), the stability of the voltage established by the AVC-MMC at the PCC (indicated as $V_{PCC}(s)$) must be assessed. $I_{PCC}(s)$ in Fig. 5 a) and $V_{PCC}(s)$ in Fig. 5 b) are given by

$$I_{PCC}(s) = V_{PCC}(s)\frac{1 + Z_p(s)/Z_g(s)}{Z_g(s)} \tag{7a}$$

$$V_{PCC}(s) = I_{PCC}(s)\frac{Z_p(s)}{1 + Z_{WF}(s)/Z_p(s)} \tag{7b}$$

Based on the impedance-based stability criteria [28], the stability of the two inter-connected system shown in Fig. 5 can be determined by applying the Nyquist criterion to $Z_p(s)/Z_g(s)$ and $Z_{WF}(s)/Z_p(s)$. If the locus does not encircle the point (-1,0), then the system is stable. This stability criterion is equivalent to that the phase difference between $Z_p(s)$ and $Z_g(s)$ or between $Z_p(s)$ and $Z_{WF}(s)$ being less than 180° at the frequency of the magnitude intersection in the Bode plot (i.e., resonance frequency). If the phase difference exceeds 180°, additional damping is required at the resonance frequency to provide positive damping to the MMC. As a consequence, the phase difference can be reduced to a value below 180°.

B. Voltage Feedforward-based Damping

The voltage feedforward-based damping control is placed in parallel (see the blue part of the diagram in Fig. 1) with the existing controllers, and the control output is sent directly to the modulator. Using multi-harmonic linearization [7] and considering up to the 3^{rd}-order steady-state harmonics, the voltage feedforward-based damping control results in adding a damping control gain matrix $\mathbf{G}_d$ to $\mathbf{P}_v$ of (3), in which $\mathbf{G}_d$ is a (7×7) diagonal matrix defined as

$$\mathbf{G}_d = \mathbf{diag}[0 \quad H_d(s - j2\omega_1) \quad 0 \quad H_d(s) \quad 0 \quad 0 \quad 0]_{7\times 7} \tag{8}$$

where $H_d(s)$ is the transfer function of damping controller. As a result, in the high-frequency range, the voltage feedforward-based damping effect is equivalent to adding $e^{-sT_d}H_d(s)$ to $N_p(s)$ in (6), and therefore the simplified admittance model of the damped MMC can be written as

$$Y_{pdv}(s) = \frac{1 + e^{-sT_d}\left[H_d(s) + G_v(s)\right]}{sL + e^{-sT_d}G_c(s)} = Y_p(s) + \frac{\overbrace{e^{-sT_d}H_d(s)}^{Y_r(s)}}{N_p(s)} \tag{9}$$

with the subscript *pdv* indicating the damped MMC impedance by voltage feedforward-based damping. Equation (9) shows that the added damping controller is independent of the other control loops used in MMC. Therefore, while this paper focuses specifically on ACC-MMC in the "V_{dc} & $Q = 0$" mode, ACC-MMC in the "P & Q" mode and AVC-MMC in single-loop "fixed V_{ac} & f" mode, the proposed damping method can also be applied to MMC with other control schemes listed in Table I. In fact, (9) can be interpreted as adding a virtual admittance $Y_r(s)$ in parallel with undamped MMC admittance $Y_p(s)$. When properly designed $H_d(s)$, the passivity of MMC at a certain frequency will be enhanced, if the designed $Y_r(s)$ has a positive real part at that frequency. As a result, this method can be referred to as the virtual admittance-based damping control. To better understand the effect of voltage feedforward damping, the circuit notation of (9) is shown in Fig. 6.

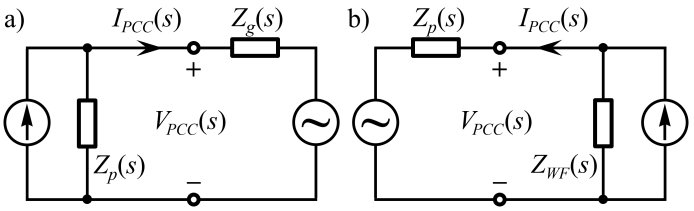

Fig. 5. Equivalent circuit of an: a) ACC-MMC connected to a grid; and b) AVC-MMC connected by wind farm;

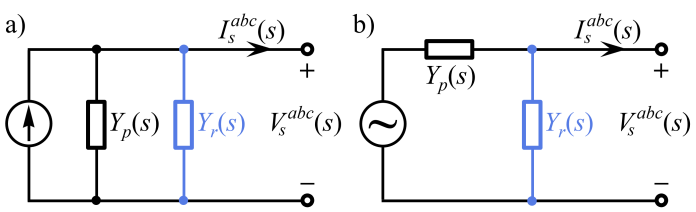

Fig. 6. Equivalent circuit of voltage feedforward-based damping for: a) MMC in ACC mode, and b) MMC in AVC mode;

C. Narrowband Damping Function $H_d(s)$

1) Phase shift of $Y_r(s)$ due to $e^{-sT_d}/N_p(s)$:

If $H_d(s)$ does not contain any filter but only a damping gain K_d, $e^{-sT_d}K_d$ in (9) will become negative in the frequency range $f \in [(4n+1)T_d/4, (4n+3)T_d/4]$, $n \in \mathbb{N}$ [29]. In addition, $1/N_p(s)$ will further add phase shift to $Y_r(s)$ (e.g., 1) For ACC-MMC in the "V_{dc} & $Q=0$" mode, the frequency response of $1/N_p(s)$ can be treated as a 2^{nd}-order bandpass filter whose center frequency roughly equals to the cutoff frequency of current control; 2) For AVC-MMC in the "single-loop fixed V_{ac} & f" mode, $1/N_p(s)$ is reduced to $1/(R_{eq}+sL_{eq})$, which provides an approximately constant -90° phase offset to $Y_r(s)$ across all the high-frequency range). As a result, $Y_r(s)$ may periodically decrease the passivity of the MMC at high frequencies when added in parallel with the MMC, leading to more oscillation issues. In order to avoid this unwanted effect, a band-pass filter must be used, in conjunction with the damping gain K_d in $H_d(s)$, to limit the damping effect provided by $Y_r(s)$ within an intended damping range.

2) Bandpass Filter in $H_d(s)$:

Various types of bandpass filters are available in the literature (see [30]), each with its own characteristics and performance specifications. Nonetheless, selecting an appropriate bandpass filter for enhancing MMC's passivity requires consideration of some critical factors, which are listed as follows:

- A higher-order filter provides a better attenuation rate below and above the intended damping range but lead to more phase shift centered on the cutoff frequency.
- The filter should be stable across all frequencies [31], and insensitive to numerical rounding errors that arise from discrete domain filter realization.
- To satisfy the damping speed requirements, the filter should have a fast settling time and a low computation burden.
- It is preferable to use a filter with polarity-selective properties allowing damping in positive or negative sequences separately.
- Methods based on the Discrete Fourier Transform (DFT) should be avoided (e.g., sliding DFT in [5]) as they require additional frequency-locked loops (FLL) to adjust the base frequency of the filter.

Based on these considerations, the first-order complex coefficient filter (CCF) [32] is adopted in this work, which is given by

$$H_{ccf}(s) = \frac{\omega_b}{s - j\omega_r + \omega_b} \tag{10}$$

where ω_r specifies the center frequency of CCF, which is also the intended frequency (e.g. resonance frequency), and ω_b defines the -3dB bandwidth. With the inclusion of CCF, the negative impact of $e^{j\theta}$ and $N_p(s)$ outside the intended damping range can be attenuated in the transition band and stop band of CCF.

3) Additional Phase Lag Compensation at ω_r:

Observe that from (9), though the phase shift effect from $e^{-sT_d}/N_p(s)$ on $Y_r(s)$ can be minimized outside the passband of CCF, $e^{j\theta}$ and $N_p(s)$ also add phase lags to $Y_r(s)$ within the passband (i.e., at and around ω_r), making $\Re\mathfrak{e}\{Y_r(j\omega_r)\}$ to be negative immediately around ω_r. To cancel the phase shift, a steady-state phase-lead compensation $e^{j\theta}$ can be included in $H_d(s)$, ensuring zero phase shift at ω_r and reducing the phase lag around it. Therefore the resulting damping controller is given by

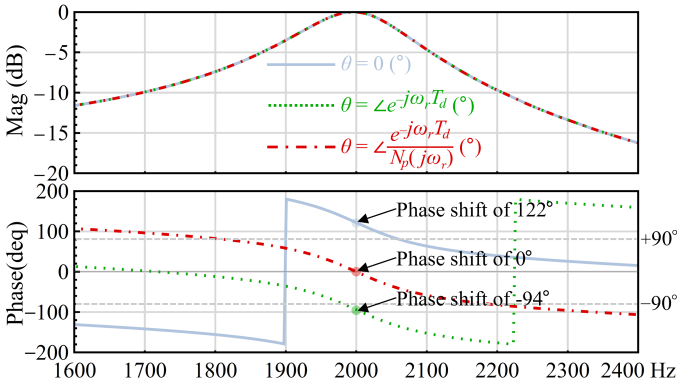

Fig. 7. Bode plots of $Y_r(s)$ centered on 2000 Hz with different choices of compensation angle

$$H_d(s) = K_d e^{j\theta} H_{ccf}(s) \tag{11}$$

where K_d is the desired damping gain. As an example of how phase lag compensation affects the passivity of $Y_r(s)$, assume that $H_d(s)$ in (11) is being designed for the ACC-MMC in the "V_{dc} & $Q=0$" mode that is described in Section II-B. $\omega_b = 2\times\pi\times80$ rad/s, $\omega_r = 2\times\pi\times2000$ rad/s, and K_d is tuned to obtain a 1 Siemens admittance at ω_r. The frequency response of $Y_r(s)$ is plotted in Fig. 7 using a linear frequency scale (zoom-in view around the selected ω_r) for different compensation angles. The one with "$\theta = 0$" indicates no phase lag compensation, the other with"$\theta = e^{-j\omega_r T_d}$" indicates that the compensation considers only the impact of time delay, while the one "$\theta = e^{-j\omega_r T_d}/N_p(j\omega_r)$" indicates a full compensation on the phase lag. As expected, with a full phase lag compensation, $Y_r(s)$ with positive real part (i.e. phase limited within [-90°, 90°]) is obtained everywhere but in a narrowband region ($f \in$ [1741 Hz, 2250 Hz]) around ω_r. $Y_r(s)$ with the negative real part is encountered outside the region, however, this could affect the passivity of the other virtual admittances located outside the region, which is the root cause of the mutual coupling between multiple virtual admittances.

IV. Virtual Admittance-Based Damping Design

With proper phase compensation at the center frequency of the CCF, the design of $H_d(s)$ is now narrowed down to the design of the damping gain K_d and the selection of the width of the damping band ω_{db}, as described in the sequel.

A. Damping Design for a Single Resonance at ω_r

1) Design Consideration of K_d:

Equation (9) and (11) can be combined and rearranged to obtain an expression that excludes K_d, as shown in (12) a), where θ is $-\angle e^{-j\omega_r T_d}/N_p(j\omega_r)$. Hence, K_d is then determined

by the conductance of undamped MMC at ω_r, resulting in (12) b), where x is a factor that scales the percentage of the total conductance of MMC being compensated at ω_r.

$$Y_d(s) = e^{j\theta}\frac{e^{-sT_d}H_{ccf}(s)}{N_p(s)} \quad a); \quad K_d = x\frac{\left|\Re\mathfrak{e}\left\{Y_p(j\omega_r)\right\}\right|}{Y_d(j\omega_r)} \quad b) \tag{12}$$

Combining (9) and (12), the designed virtual admittance can be re-written as:

$$Y_r(s) = K_d Y_d(s) = K_d e^{j\theta}\frac{e^{-sT_d}H_{ccf}(s)}{N_p(s)} \tag{13}$$

2) Design Consideration of x:

As indicated in (12) b), x can be treated as a per-unit (p.u.) value, which expresses the designed amount of conductance (i.e., $\Re\mathfrak{e}\{Y_r(j\omega_r)\}$) in terms of a base quantity selected as conductance of undamped MMC (i.e., $\Re\mathfrak{e}\left\{Y_p(j\omega_r)\right\}$). Theoretically, x can be any value greater than 0. However, adding a positive conductance at ω_r would cause a change in MMC magnitude at ω_r, indicating a new magnitude intersection between the damped MMC impedance and ac system impedance. As a result, a new resonance may be developed if the new resonance frequency falls into the non-passive region. As depicted in Fig. 8 a), $x = 1$ gives improved passivity, as it helps to fully cancel the negative conductance of MMC at ω_{r1} (i.e., $\Re\mathfrak{e}\{Y_p(j\omega_{r1})\}$). But it is often not enough to prevent instability, as the compensation makes the damped MMC purely inductive. In turn, this decreases the magnitude of MMC's admittance at ω_{r1}, and as a result, it moves the resonance frequency above the original resonance frequency ω_{r1}, at which system net-damping may still be negative. To avoid resonance frequency drift, x can be set to 2 to ensure that $\left|Y_{pdv}(j\omega_r)\right| = \left|Y_p(j\omega_r)\right|$. This design approach is illustrated in Fig. 8 b), where the magnitude of MMC admittance remains unchanged before and after damping.

As shown in Fig. 7, the designed virtual admittance $Y_r(s)$ introduces a positive real admittance below ω_r and above ω_r, but only within a narrow damping band where the phase response of $Y_r(s)$ is inside $[-90°, 90°]$. Thus, the passivity of the MMC is enhanced within this narrow frequency range centered at ω_r, which allows system resonance frequency to move slightly below or above ω_r after damping. As a result, one can further enlarge x to effectively adjust the level of damping introduced based on the system damping requirements.

3) Width of the Damping Band ω_{db}:

For design purposes, we first define the term damping band ω_{db} to be the frequency range around ω_r where the phase response of $Y_r(s)$ is inside [-90°, 90°]. If one ignores $e^{j\theta}e^{-sT_d}$ and $1/N_p(s)$ in (13), then ω_{bd} would be the entire frequency range, as the phase shift of the 1^{st}-order CCF is always within $[-90°, 90°]$. However, $e^{-sT_d}e^{j\theta}$ and $N_p(s)$ further enlarge the phase shift. Given the -3dB bandwidth ω_b and center frequency ω_r of $H_{ccf}(s)$, the width of damping band ω_{db} can be obtained by numerically evaluating the following expressions

$$\begin{cases} \omega_l = \mathbf{max}\{\mathsf{FindRoot}[\frac{e^{j\omega_r T_d}e^{-j\omega T_d}H_{ccf}(j\omega)}{N_p(j\omega)} = 0, x \le \omega_r]\} \\ \omega_u = \mathbf{min}\{\mathsf{FindRoot}[\frac{e^{j\omega_r T_d}e^{-j\omega T_d}H_{ccf}(j\omega)}{N_p(j\omega)} = 0, x \ge \omega_r]\} \\ \omega_{db} = \omega_u - \omega_l \end{cases} \tag{14}$$

where, FindRoot denotes a function returns the roots of the polynomial represented by $e^{j\omega_r T_d}e^{-j\omega T_d}H_{ccf}(j\omega)/N_p(j\omega)$, which can be programmed in any available numerical computing environment.

As mentioned previously, if x is selected to be greater than 2, the virtual admittance would cause $|Y_{pdv}(j\omega_r)| > |Y_p(j\omega_r)|$, leading to a resonance frequency drift. In general, after K_d is obtained, ω_{db} can be selected as any value as long as it is wide enough to cover the drifted resonance frequency. However, though a large ω_{db} increases the passivity of MMC over a wider frequency range centered on ω_r, it can result in unintended effects at other frequencies nearby the damping band.

B. Damping Design for Multiple Resonances from ω_{r1} to ω_{rn}

The proposed damping controller design may be applied to more than one resonance frequency in two scenarios: 1) There are multiple magnitude intersections between impedance of MMC and the impedance of external system, where the net-damping at each intersection are all smaller than zero. As a result, there are multiple resonances in the system that need to be suppressed simultaneously; 2) There are multiple magnitude intersections between the impedance of MMC and the impedance of external system, but the negative net-damping exits only at some intersection frequencies. However, the added virtual admittances that enhance passivity at those frequencies may induce new resonances at other frequencies where the MMC was poorly damped in the first place.

1) Mutual Coupling Effect:

To better understand the mutual coupling effect, consider an example where virtual admittances $Y_{r2}(s)$, $Y_{r3}(s)$, …, $Y_{rn}(s)$ are designed to enhance passivity at ω_{r2}, ω_{r3}, …, ω_{rn}. Each $Y_{rk}(s)\ \forall\, k = 2\ldots n$ introduces an admittance at ω_{r1}, which are

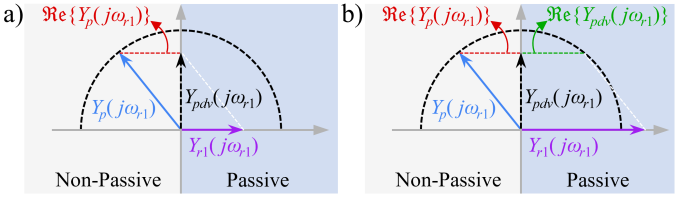

Fig. 8. Complex vector figure of the admittances at ω_{r1} under single-tuned damping when a) $x = 1$; b) $x = 2$.

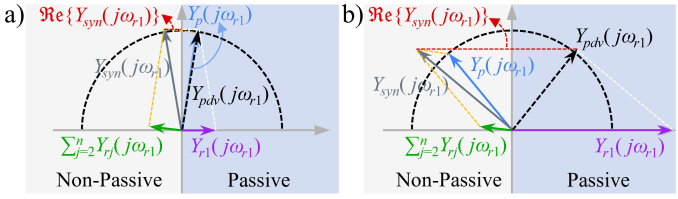

Fig. 9. Complex vector figure of admittances at ω_{r1} under multi-tuned damping when undamped MMC admittance a) $Y_p(j\omega_{r1}) > 0$; b) $Y_p(j\omega_{r1}) < 0$

$Y_{r2}(j\omega_{r1})$, $Y_{r3}(j\omega_{r1})$, …, $Y_{rn}(j\omega_{r1})$. All of these admittances can be superposed and denoted as $\sum_{j=2}^{n} Y_{rj}(j\omega_{rj})$. Fig. 9 a) illustrates the complex vector of admittances at ω_{r1}, where $Y_p(j\omega_{r1})$ is the undamped MMC impedance at ω_{r1}. As can be observed, even if $Y_p(j\omega_{r1})$ is passive, the impedance $Y_{syn}(j\omega_{r1})$ synthesized by $\sum_{j=2}^{n} Y_{rj}(j\omega_{rj})$ and $Y_p(j\omega_{r1})$ falls into the non-passive range. There is, therefore, a risk of the occurrence of a new unstable resonance at ω_{r1} after damping controllers are applied at ω_{r2}, ω_{r3}, …, ω_{rn}. On the other hand, as depicted in Fig. 9 b), when an MMC's impedance is originally non-passive at ω_{r1}, the MMC's passivity at ω_{r1} can be further jeopardized by $\sum_{j=2}^{n} Y_{dj}(j\omega_{rj})$ (i.e., $\mathfrak{Re}\{Y_{syn}(j\omega_{r1})\} < \mathfrak{Re}\{Y_p(j\omega_{r1})\} < 0$). Therefore, the design of the virtual admittance at a particular resonance frequency should also counteract the negative conductance introduced by the virtual admittances centered at other resonance frequencies.

2) Design Consideration of Damping Gains K_{dk}:

Assume that virtual admittances $Y_{rk}(s)|_{k=1,\ldots,n}$ needs to be designed at $\omega_{rk}|_{k=1,\ldots,n}$, and x for each virtual admittance is selected to be $x_k|_{k=1,\ldots,n}$. Considering the full effects of mutual coupling on the designed admittance at each intended frequency, a proper design of K_{dk} yields:

$$\begin{cases} \underbrace{K_{d1}Y_{d1}(j\omega_{r1})}_{Y_{r1}(j\omega_{r1})} + \underbrace{\sum_{k=2}^{n} K_{dk}Y_{dk}(j\omega_{r1})}_{\text{Mutual Coupling Effect at } \omega_{r1}} = \underbrace{x_1 \left|Y_p(j\omega_{r1})\right|}_{\text{Desired Conductance}} \\ \underbrace{K_{d2}Y_{d2}(j\omega_{r2})}_{Y_{r2}(j\omega_{r2})} + \underbrace{\sum_{k\neq 2}^{n} K_{dk}Y_{dk}(j\omega_{r2})}_{\text{Mutual Coupling Effect at } \omega_{r2}} = \underbrace{x_2 \left|Y_p(j\omega_{r2})\right|}_{\text{Desired Conductance}} \\ \vdots \\ \underbrace{K_{dn}Y_{dn}(j\omega_{rn})}_{Y_{rn}(j\omega_{rn})} + \underbrace{\sum_{k=1}^{n-1} K_{dk}Y_{dk}(j\omega_{rn})}_{\text{Mutual Coupling Effect at } \omega_{rn}} = \underbrace{x_n \left|Y_p(j\omega_{rn})\right|}_{\text{Desired Conductance}} \end{cases} \tag{15}$$

where $Y_{dk}(s)$ is in the same expression to $Y_d(s)$ in (12) a). By putting such system of linear equations into matrix form, the damping gains can be solved by calculating

$$\boldsymbol{K}_d = \begin{bmatrix} \mathfrak{Re}\{\mathbf{Y}_{dk}(j\omega_{r1})\} \\ \mathfrak{Re}\{\mathbf{Y}_{dk}(j\omega_{r2})\} \\ \vdots \\ \mathfrak{Re}\{\mathbf{Y}_{dk}(j\omega_{rn})\} \end{bmatrix}^{-1} \cdot \mathrm{diag}(x_k) \cdot \begin{bmatrix} \left|\mathfrak{Re}\{Y_p(j\omega_{r1})\}\right| \\ \left|\mathfrak{Re}\{Y_p(j\omega_{r2})\}\right| \\ \vdots \\ \left|\mathfrak{Re}\{Y_p(j\omega_{rn})\}\right| \end{bmatrix} \tag{16}$$

where, $k = 1, 2, ..., n$; $\boldsymbol{K}_d = [K_{d1}, K_{d2}, ..., K_{dn}]^{\mathrm{T}}$; $\mathbf{Y}_{dk}(j\omega_{rk})$ are row vectors with n entries; $\mathrm{diag}(x_k)$ is a $(n \times n)$ diagonal matrix, consisting of elements that are specified by the desired amount of positive conductance in p.u. at resonance frequencies $\omega_{rk}|_{k=1,\ldots,n}$.

3) Determination of x_k:

When $Y_p(j\omega_{rk})$ is negative at ω_{rk}, the same considerations on selection of x_k as discussed in Section IV-A can be applied. Special attention must be paid when the MMC admittance originally has a positive real part at a certain intended frequency ω_{rk}, but the mutual coupling effects lead to a negatively damped admittance at that frequency after damping controls are applied to enhance passivity at other frequencies. In such a condition, $x_k = 1$ is recommended for virtual admittance designed at ω_{rk} unless a specific damping level is required, which maintains the original passivity of MMC at ω_{rk} and avoids creating a new unstable resonance.

4) Existence of Solutions for $\boldsymbol{K}_d$:

Equation (16) can be written in a shortened form as:

$$\boldsymbol{K}_d = \mathbb{Y}^{-1}\mathbb{X}\boldsymbol{b} \tag{17}$$

As $\boldsymbol{K}_d$ is calculated by using the inverse of $\mathbb{Y}$, it is necessary to discuss the condition for $\mathbb{Y}$ to be an inverse-positive matrix, and to provide the solution when $\mathbb{Y}$ is not inverse-positive.

In order to understand the characteristics of the entries in $\mathbb{Y}$, one may recall Fig. 7 and re-plot the $Y_r(s)$ with a full phase lag compensation in a wider frequency range from 100 Hz to 5 kHz, as shown in Fig. 10. As can be seen, the added virtual admittance creates a narrow positive damping range (i.e., Region 1) around 2 kHz, but outside this range unwanted negative damping is added almost everywhere except Region 2 and 3. Therefore, $\mathbb{Y}$ is usually a *Z-matrix* whose off-diagonal entries are less than or equal to zero [33]. In addition, the added virtual admittance designed for intended frequencies (i.e., main-diagonal entries) is strictly conductive and positive. Hence, based on the *Gershgorin Circle Theorem* [34], the eigenvalues of $\mathbb{Y}$ are all positive, which indicates that $\mathbb{Y}$ is a non-singular *M-matrix* whose inverse matrix is always positive [33].

In case another intended frequencies fall within the Region 2 or Region 3, though it is not usual, there will be positive entries in $\mathbb{Y}$, meaning $\mathbb{Y}$ is not a non-singular *M-matrix*. However, from the perspective of passivity enhancement of MMC, the positive entry represents that: When a virtual admittance $Y_r(s)$ centered at 2 kHz is introduced, there is always positive damping inherently added to Region 2 and Region 3, enhancing the passivity of MMC in these two regions. It should be noted that the amount of positive damping introduced by $Y_r(s)$ to Region 2 and Region 3 is relatively small, as a result of the magnitude attenuation of the bandpass filter used in the damping controller. Thus, a simple and direct solution is to replace these positive entries in $\mathbb{Y}$ by 0, then $\mathbb{Y}$ becomes to a non-singular *M-matrix* and it is again inverse-positive.

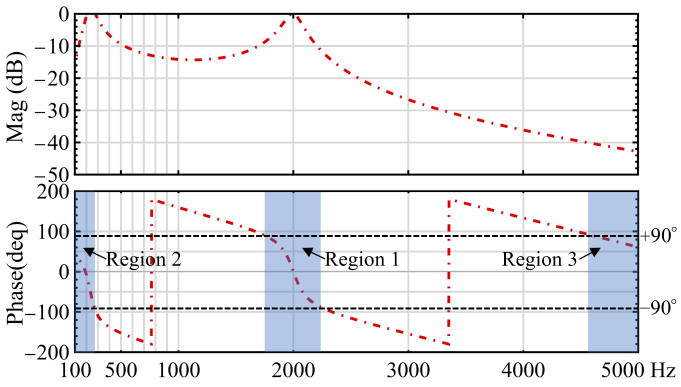

Fig. 10. Bode plots of $Y_r(s)$ centered on 2000 Hz with a full phase lag compensation

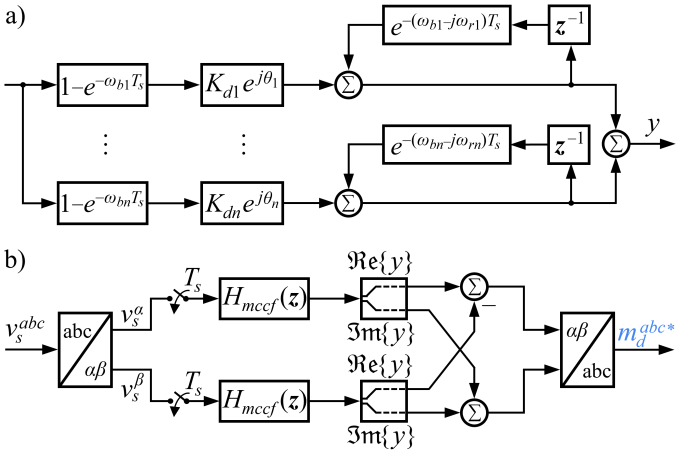

Fig. 11. The structure of MCCF synthesized as direct-form I; b) realization of the proposed voltage feedforward-based damping in $\alpha\beta$ reference frame

C. Discrete-Time Modeling of the Proposed Damping Controller

Due to the discrete nature of measurements, controls and modulation, a CCF in the z-domain, synthesized as direct-form I [31], is adopted in this work. With its multiple-parallel expression, multiple CCF (MCCF) can be synthesized simultaneously, as shown in Fig. 11 a). The transfer function of discretized MCCF is given by

$$H_{mccf}(z) = \sum_{k=1}^{n} \frac{K_{dk} e^{j\theta_k}(1 - e^{-\omega_{bk} T_s})z}{z - e^{-(\omega_{bk} - j\omega_{rk})T_s}} \tag{18}$$

It is noteworthy that $e^{-\omega_{bk}T_s}$, $e^{j\omega_{rk}T_s}$ and $e^{j\theta_k}$ in (18) result in complex-valued signals, while practical signals are real-valued. Hence, to make use of the imaginary part of complex-valued signals, the realization of the proposed damping control is accomplished in the $\alpha\beta$-reference frame [32] as shown in Fig. 11 b), where three-phase voltage v_s^{abc} is the input, and the damping controller output m_d^{abc} is directly sent to the MMC modulator as early illustrated in Fig. 1.

The block diagram in Fig. 12 offers a comprehensive overview of the process for programming the proposed multi-tuned narrowband damping control, drawing upon the discussions and findings presented throughout the paper. This high-level architecture captures the key stages involved in developing the damping control method, beginning with the identification of high-frequency oscillations and continuing through to the final implementation of the multi-tuned narrowband damping control strategy.

V. Case Studies

To validate the performance of the proposed narrowband damping method on suppressing HFO in MMC-based applications, three examples are presented in this section. For the sake of illustration of proposed damping control in the forthcoming examples, the resonance frequencies are assumed to be given by online resonance detection or online impedance measurement method such as those in [21]–[23]. The MMC-based renewable energy integration has been known to suffer from multiple HFOs when the MMC is imposed to long overhead transmission lines (OTL) or HVac cables [5], [21]. The first two case studies specifically aim to verify the performance of the multiple narrowband damping method in a scenario when the ACC-MMC is connected to a 160-km overhead transmission line (OTL) via a 300/345 kV step-up transformer, where in the first case the MMC operates in V_{dc} & $Q = 0$ mode while the MMC in the second cases works in P & Q mode. The third case study aims to validate the performance of the proposed narrowband damping controls when used to suppress HFO during the integration of wind farms. Each of the case is simulated in MATLAB/Simulink using a detailed EMT models, inclusive of the MMC.

A. ACC-MMC (V_{dc} & $Q = 0$) Connected to a Long Overhead Transmission Line

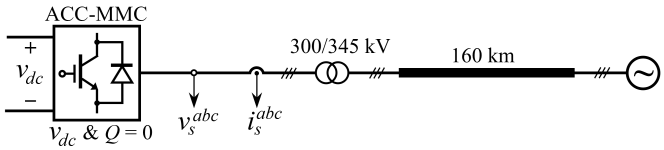

Fig. 13. ACC-MMC (V_{dc} & $Q = 0$ mode) connected to a power grid via 160-km long overhead transmission line.

The ACC-MMC is connected to a 345 kV OTL via a 300/345 kV step-up transformer. The OTL has a length of 160 km and the parameters are tabulated in Table IV. The power grid behind the transmission line is assumed to be an ideal voltage source. The schematic diagram of this system is depicted in Fig. 13.

TABLE IV
PARAMETERS OF THE 345 KV OTL

Parameter	Series Resistance	Series Inductance	Shunt Capacitance
Values (per km)	18.45×10^{-3} Ω	0.98×10^{-3} H	11.06×10^{-9} F

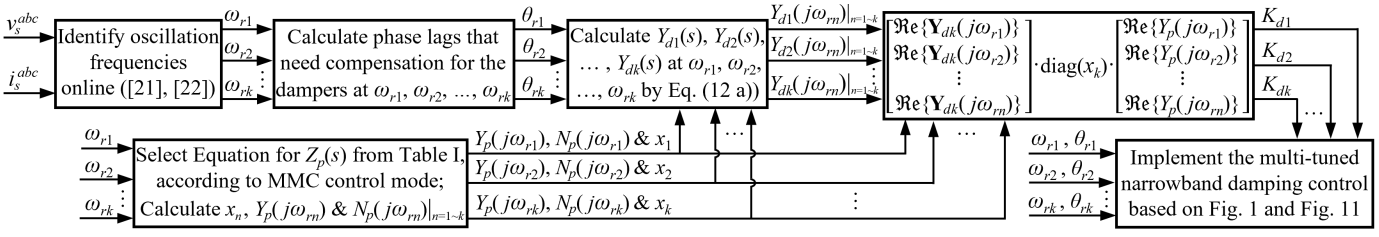

Fig. 12. The big-picture architecture of the programming of the multi-tuned damping control.

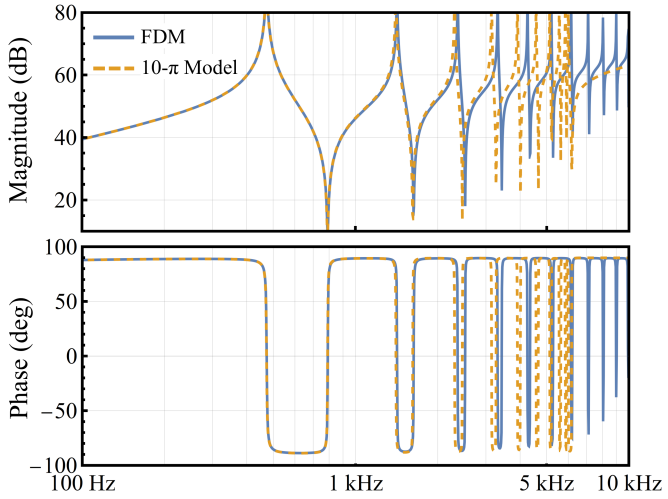

Fig. 14. Impedance responses of 160 km, 345 kV OTL predicted by frequency-dependent model and 10 cascaded π-sections

1) Modeling of Long Transmission Line

The impedance of a long transmission lines exhibit multiple peaks (i.e., shunt resonances) and dips (i.e., series resonances) on the magnitude due to the distributed nature of the line. To correctly predict the high-frequency characteristic of a long transmission line, cascaded π-section models are widely used in the literature [4], [16]. However, the number of π-sections needed depends on the targeted analysis frequency range and the desired level of accuracy. As an example, the impedance comparison of the 160-km OTL predicted by 10 cascaded π-section model and predicted by the frequency-dependent model (FDM) [35] is given in Fig. 14. As can be observed from the comparison, a 10 π-section model can only approximate the high-frequency behavior of the OTL up to 2 kHz. Although a larger number of π sections can help predict the high-frequency impedance of a long transmission line more precisely, adding more π-sections inevitably reduces simulation efficiency, and might even cause spurious numerical oscillations [36]. Considering that the targeted frequency range in this work ranges from 100 Hz to the Nyquist frequency (i.e., 5000 Hz), the FDM-based OTL model is adopted and used in the remaining examples.

2) Impedance Analysis and Simulation Validation

Fig. 15 shows the impedance response of the undamped MMC impedance $Z_p(s)$ (orange), the impedance of MMC with five damping controllers (i.e., penta-tuned damping) $Z_{p5d}(s)$ (green) and the OTL impedance $Z_g(s)$ (blue). The undamped MMC and OTL result in five series resonances below 5 kHz at 724 Hz, 1551 Hz, 2448 Hz, 3372 Hz, and 4305 Hz. Table V summarizes the undamped MMC's damping (marked as $\mathfrak{Re}\{Z_p(s)\}$), damped MMC's damping (marked as $\mathfrak{Re}\{Z_{p5d}(s)\}$) and the phase difference between $Z_p(s)$ and $Z_g(s)$, and between $Z_{p5d}(s)$ and $Z_g(s)$. As indicated by the green box in the second row of Table V, the MMC is negatively damped at 1551 Hz, 2448 Hz and 3372 Hz where the real part of the MMC impedance is negative. Thanks to the resistance of the step-up transformer and the resistance

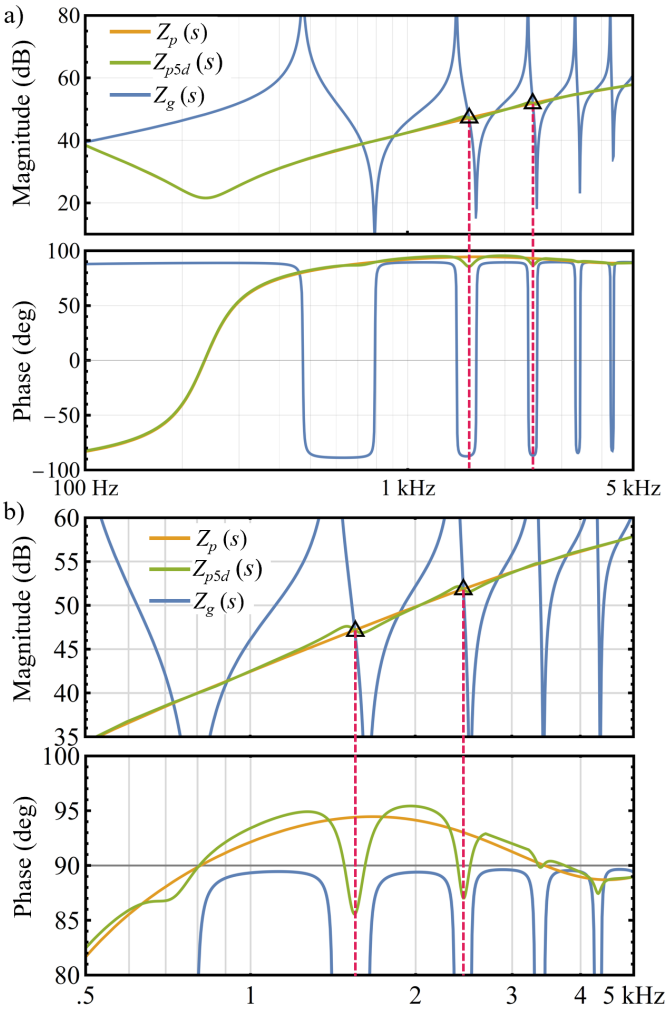

Fig. 15. a) Impedance responses of: undamped and damped ACC-MMC (V_{dc} & $Q=0$ mode) against OTL impedance; b) zoom-in view of impedance responses plotted in a).

distributed along the OTL, only the phase difference at 1551 Hz exceeds 180°, while with the phase difference at 2448 Hz is very close to 180°. According to the impedance-based stability theory, an unstable oscillations at 1551 Hz and poorly damped oscillations at 2448 Hz are expected when this MMC connects to the OTL.

Although it is not necessary to design damping controllers for all resonance frequencies listed in Table V, it is important to demonstrate the ability of the method to address multiple resonance frequencies simultaneously over a wide frequency range. The compensation angle used in (12) for the damping

TABLE V
MMC'S DAMPING AND PHASE DIFFERENCE AT INTERSECTION FREQUENCIES (CASE 1)

	724 Hz	1551 Hz	2448 Hz	3372 Hz	4305 Hz
$\mathfrak{Re}\{Z_p(s)\}$	2.21 Ω	−17.54 Ω	−20.62 Ω	−1.63 Ω	15.22 Ω
$\angle Z_p(s) - \angle Z_g(s)$	176.52°	181.65°	179.81°	174.62°	171.27°
$\mathfrak{Re}\{Z_{p5d}(s)\}$	4.45 Ω	17.62 Ω	20.37 Ω	1.63 Ω	30.73 Ω
$\angle Z_{p5d}(s) - \angle Z_g(s)$	175.06°	172.83°	173.80°	174.28°	169.98°

controller at each frequency is calculated by substituting the resonance frequencies into $\theta = -\angle e^{-j\omega_r T_d}/N_p(j\omega_r)$, which yields θ = [140.68°,-153.92°,-90.73°,-27.05°,38.69°]. Thereafter, the damping gain of each damping controller can be automatically obtained by using a suitable computer program to solve the following matrix equation [2]

$$\boldsymbol{K}_d = \mathbb{Y}^{-1}\mathbb{X}\boldsymbol{b} \tag{19}$$

where

$$\mathbb{Y} = \begin{bmatrix} 113.24 & -9.43 & -4.25 & 0.63 & 2.46 \\ -3.51 & 42.09 & -3.17 & -1.52 & 0.23 \\ -0.86 & -1.74 & 23.04 & -1.70 & -0.79 \\ 0.08 & -0.54 & -1.10 & 14.98 & -1.12 \\ 0.23 & 0.06 & -0.36 & -0.77 & 10.54 \end{bmatrix} \times 10^{-4}$$
$$\xrightarrow{min(\mathbb{Y},0)} \begin{bmatrix} 113.24 & -9.43 & -4.25 & 0 & 0 \\ -3.51 & 42.09 & -3.17 & -1.52 & 0 \\ -0.86 & -1.74 & 23.04 & -1.70 & -0.79 \\ 0 & -0.54 & -1.10 & 14.98 & -1.12 \\ 0 & 0 & -0.36 & -0.77 & 10.54 \end{bmatrix} \times 10^{-4} \tag{20}$$

$$\mathbb{X} = \begin{bmatrix} 1 & 0 & 0 & 0 & 0 \\ 0 & 2 & 0 & 0 & 0 \\ 0 & 0 & 2 & 0 & 0 \\ 0 & 0 & 0 & 2 & 0 \\ 0 & 0 & 0 & 0 & 1 \end{bmatrix} \quad \text{and} \quad \boldsymbol{b} = \begin{bmatrix} 2.89 \\ 6.73 \\ 2.68 \\ 0.11 \\ 0.32 \end{bmatrix} \times 10^{-4} \tag{21}$$

which yields $\boldsymbol{K}_d = [0.044, 0.174, 0.134, 0.026, 0.035]^{\mathrm{T}}$. It should be noted that, based on the discussion in the Section IV.B.*4)*, in order to ensure matrix $\mathbb{Y}$ always invertible, the positive entry in $\mathbb{Y}$ is automatically replaced by 0 as shown in (20) (e.g., MATLAB command $\mathsf{min}(\mathbb{Y},0)$). It is also worth mentioning that each element of matrices (19), (20) and (21) are automatically calculated by a computer program when the resonance frequencies are given.

Fig. 15 demonstrates that the designed penta-tuned damper has negligible effect on the impedance, except in the immediate vicinity of the damping band created by each damping controller. Table V shows that the added damper reduces the phase differences at 1551 Hz and 2448 Hz to 172.83° and 173.80°, respectively, indicating that both the negatively damped and poorly damped impedance are compensated. In particular, as noted by the green box in the fourth row of Table V, the designed damper introduced the expected level of positive damping, which compensates the negative MMC damping at 1551 Hz, 2448 Hz and 3372 Hz while virtually not changing the absolute value of the real part of the MMC impedance at these frequencies. As a consequence, the magnitude intersection frequencies between MMC and OTL remain unchanged before and after damping.

Time-domain simulation results are presented in Fig. 16 a) and b) to verify the performance of the penta-tuned damping control design. The simulation is carried out by connecting the undamped MMC to the OTL, resulting in an unstable oscillation that arises at 1551 Hz. At t = 0.5 s, the penta-tuned damping control is enabled, and the growing oscillation is effectively suppressed within five fundamental cycles, allowing MMC to transfer power to the power grid stably. At t = 2.5 s, the added penta-tuned damping function is deactivated, causing the 1551 Hz oscillation to grow once again.

[2]Note: the cutoff frequency ω_{bk} is set to be $2\pi \cdot 80$ rad/s for each CCF.

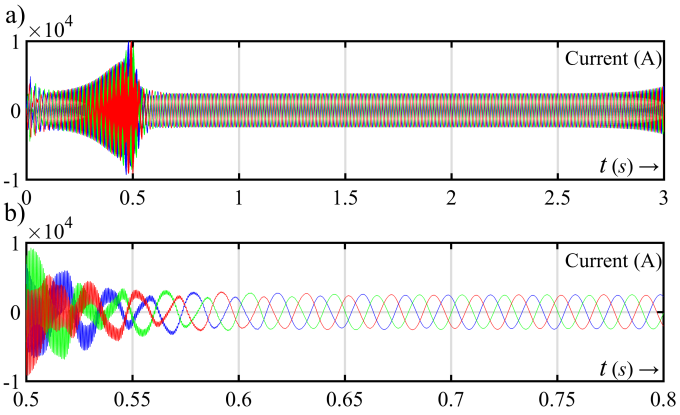

Fig. 16. Simulated time-domain responses: a) overall response of MMC current; b) zoom-in view of MMC current in 0.5 ∼ 0.8s

B. ACC-MMC (P & Q Mode) Connected to a Long Overhead Transmission Line

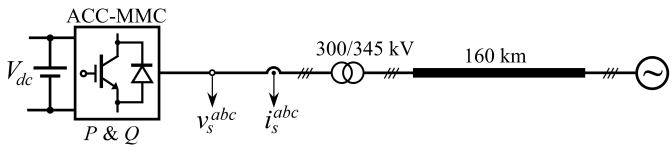

Fig. 17. ACC-MMC (*P* & *Q* mode) connected to a power grid via 160-km long overhead transmission line.

As indicated by Table I and Fig. 3, the outer active/reactive power loop contributes to positive damping for the frequency range below 1 kHz, helping the MMC to avoid oscillation in that region. However, the outer active/reactive power loop levels up the amount of negative damping between 1 kHz and 3 kHz, a frequency range where the majority of reported HFO issues occur [3], [4]. This subsection specifically aims to verify the multi-tuned narrowband damping method when a *P* & *Q* controlled MMC is connected to the OTL defined in case 1, and to demonstrate the generality of our proposed damping method.

Fig. 18 displays the undamped MMC impedance $Z_p(s)$ (orange), the damped MMC impedance $Z_{p3d}(s)$ (green) and their comparison with the OTL impedance $Z_g(s)$ (blue). The MMC forms series resonances with the OTL at five frequencies listed in Table VI, where the damping of $Z_p(s)$ and the phase difference between $Z_p(s)$ and $Z_g(s)$ are also presented. As shown in Table VI, $Z_p(s)$ exhibits negative damping at 1559 Hz, 2448 Hz and 3369 Hz, with the phase differences at 1559 Hz and 2448 Hz larger than 180°. This results in two

TABLE VI
MMC'S DAMPING AND PHASE DIFFERENCE AT INTERSECTION FREQUENCIES (CASE 2)

	747 Hz	**1559 Hz**	**2448 Hz**	**3369 Hz**	**4303 Hz**
$\mathfrak{Re}\{Z_p(s)\}$	16.07 Ω	−38.95 Ω	−63.75 Ω	−18.63 Ω	48.72 Ω
$\angle Z_p(s) - \angle Z_g(s)$	159.58°	188.5°	185.99°	176.27°	168.65°
$\mathfrak{Re}\{Z_{p3d}(s)\}$	13.36 Ω	40.15 Ω	62.07 Ω	18.34 Ω	37.38 Ω
$\angle Z_{p3d}(s) - \angle Z_g(s)$	162.62°	165.48°	167.72°	172.67°	169.59°

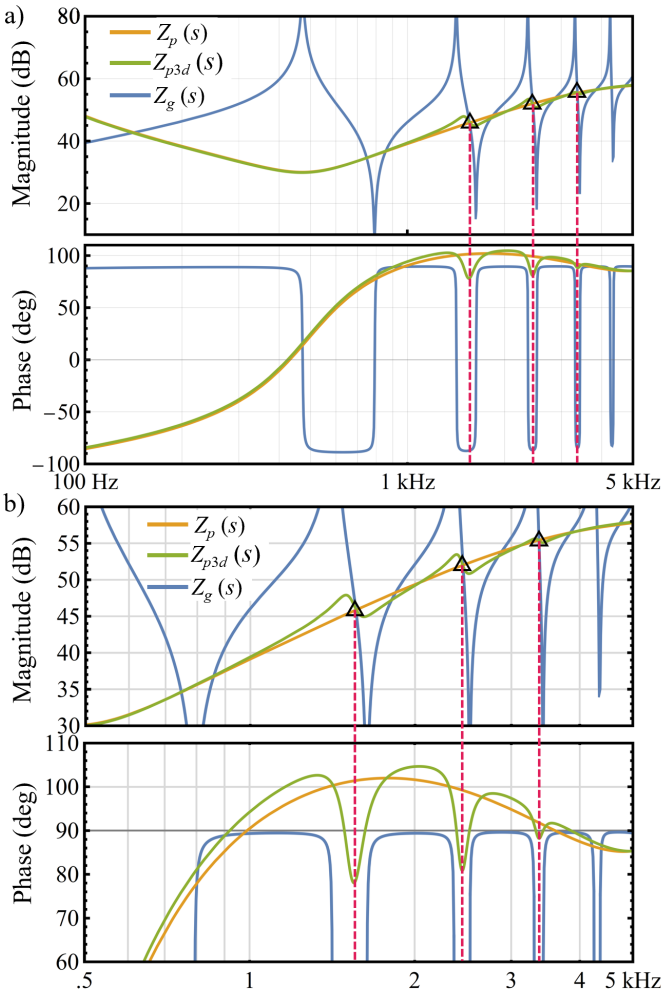

Fig. 18. a) Impedance responses of: undamped and damped ACC-MMC (P & Q mode) against OTL impedance; b) zoom-in view of impedance responses plotted in a).

unstable oscillations, with the one at 1559 Hz dominating due to its larger phase difference.

In contrast to Case 1, $Z_p(s)$ has sufficient positive damping around 747 Hz and 4303 Hz. Thus, narrowband damping in this case targets only the three aforementioned frequencies where the MMC is negatively damped. Because the design process follows the method discussed in Section IV and the calculation of damping gain is similar to what was presented in Case 1, the details of the calculation process are omitted here for the sake of briefness. The damping gains $\boldsymbol{K}_d$ obtained with the proposed design method are $\boldsymbol{K}_d = [0.4467, 0.3956, 0.1218]^{\mathrm{T}}$ for this case.

As it can be observed in Fig. 18 and Table VI, the triple-tuned damper reduces the phase difference between $Z_p(s)$ and $Z_g(s)$ ∼23° at 1559 Hz, ∼18° at 2448 Hz and ∼4° at 3368 Hz, effectively eliminating the negative damping of the MMC at all three resonance frequencies. In addition, the designed damper results in a negligible phase boost at 747 Hz and 4303 Hz, demonstrating that narrowband damping has minimal effects on the impedance shape of the MMC at unintended frequencies.

The above analysis and damping performance has been validated via time-domain simulation and the results are presented in Fig. 19. The simulation is conducted by connecting the MMC to the OTL without the triple-tuned dampers conducted. The system experiences an immediate and unstable oscillation due to the 188.5° phase difference at 1559 Hz, and within 150 ms, the currents in the system exceed the rated MMC current more than 4.5 times. The proposed triple-tuned damper is activated at 0.15 s to suppress the oscillation, and the unstable oscillation disappears at 0.4 s. At t = 2.7 s, the added triple-tuned damping function is deactivated, causing the 1559 Hz oscillation to grow once again. Note that, in a real-world practical application where such a severe unstable oscillation scenario may arise, it is critical to have an online resonance detection scheme with fast response to identify the oscillation frequency and provide it for damping control.

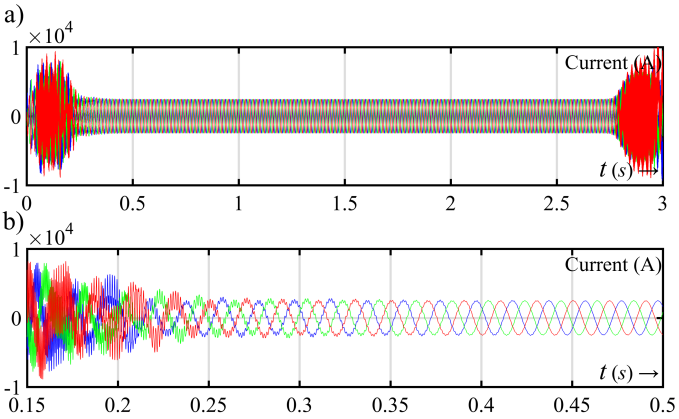

Fig. 19. Simulated time-domain responses: a) overall response of MMC current; b) zoom-in view of MMC current in 0.15 ∼ 0.5s

C. AVC-MMC Connected by a Wind Farm

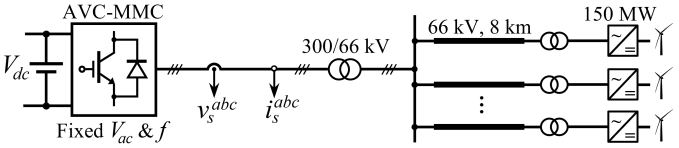

Fig. 20. MMC-based offshore wind integration through 8-km short submarine cable networks.

The third case study aims to illustrate the proposed multiple narrowband damping control when used to suppress the oscillations between the AVC-MMC and a wind farm during MMC-based wind integration (Note that the MMC in this case does not use dual loop). In the wind farm, there are six 8-km cable strings rated at 66 kV (RMS ph-ph), and the terminal of each string is connected by an aggregated 150 MW Type-IV turbine interfaced via a 0.69/66 kV (RMS ph-ph) step-up transformer. The six strings are collected and the voltage is stepped up to 300 kV (RMS ph-ph) to interconnect with the MMC. A 2.5 kHz double-edged sampling-based PWM (resulting in a 100 μs delay), and 200 μs digital control delay are additionally included in the Type-IV turbine model. It should be noted that, for demonstration purposes, this 200 μs digital control delay is added into the wind turbine controller to create a negatively

TABLE VII
MMC'S DAMPING AND PHASE DIFFERENCE AT INTERSECTION FREQUENCIES (CASE 3)

	218 Hz	583 Hz
$\mathfrak{Re}\{Z_p(s)\}$	−2.90 Ω	−16.06 Ω
$\angle Z_p(s) - \angle Z_{WF}(s)$	180.09°	192.28°
$\mathfrak{Re}\{Z_{p2d}(s)\}$	40.15 Ω	62.07 Ω
$\angle Z_{p2d}(s) - \angle Z_{WF}(s)$	166.02°	164.47°

damped wind farm impedance in the medium frequency range. The schematic diagram of the system is depicted in Fig. 20.

Fig. 21 compares the impedance response of the undamped MMC $Z_p(s)$ and the wind farm $Z_{WF}(s)$ above 100 Hz, the MMC and the wind farm form two series resonances at 218 Hz and 583 Hz, where the damping of $Z_p(s)$ and the phase difference between them are also presented. As shown in Table VII, $Z_p(s)$ is negatively damped at both 218 Hz and 583 Hz, with the phase difference of 180.08° and 192.28° between it and $Z_{WF}(s)$, respectively. As a consequence, it can be inferred that two unstable oscillations would arise at 218 Hz and 583 Hz, with 583 Hz being the dominant frequency.

Note that the resonance frequency 218 Hz is close to the near-synchronous range (i.e., below $\sim$ 100 Hz), which is where most of the controls' bandwidth are located. To avoid unintended stability issues at low frequencies, a CCF with short bandwidth is needed to limit the damping control effect to a relatively narrow range around 218 Hz. In this case, the cutoff frequency of the CCF centering at 218 Hz is designed to be ω_{b1} = 5 Hz, and the cuttoff frequency of CCF at 583 Hz to be ω_{b2} = 30 Hz. diag(x_k) is defined by diag(2, 2) as the MMC is negatively damped at both frequencies. The solution of $\boldsymbol{K}_d$ is [0.39, 0.70].

The impedance response of MMC damped by double-tuned damping (marked as $Z_{p2d}(s)$) is also plotted in Fig. 21, and the phase difference between $Z_{p2d}(s)$ and $Z_{WF}(s)$ at 218 Hz and 583 Hz are pulled down to 166.02° and 164.47° (see Table VII). As a result, the unstable oscillations are expected to be damped at both frequencies, and a stable operation of the wind farm can be ensured.

Above analysis is confirmed by the time-domain simulation results presented in Fig. 22, where the simulation is started with 200 μs control delay excluded from turbine controller except 100 μs PWM delay, thus a stable operation of the MMC-wind farm is observed. At t = 0.4 s, the 200 μs control delay is added to the turbine controller, and unstable oscillations dominated by the 583 Hz resonance are created. The designed double-tuned virtual admittance is enabled at t = 0.5 s and the fast-growing oscillation is quickly mitigated within two fundamental cycles. At t = 2.8 s, the double-tuned virtual admittance is deactivated, and the resonance at 583 Hz pushes the unstable oscillation to grow again.

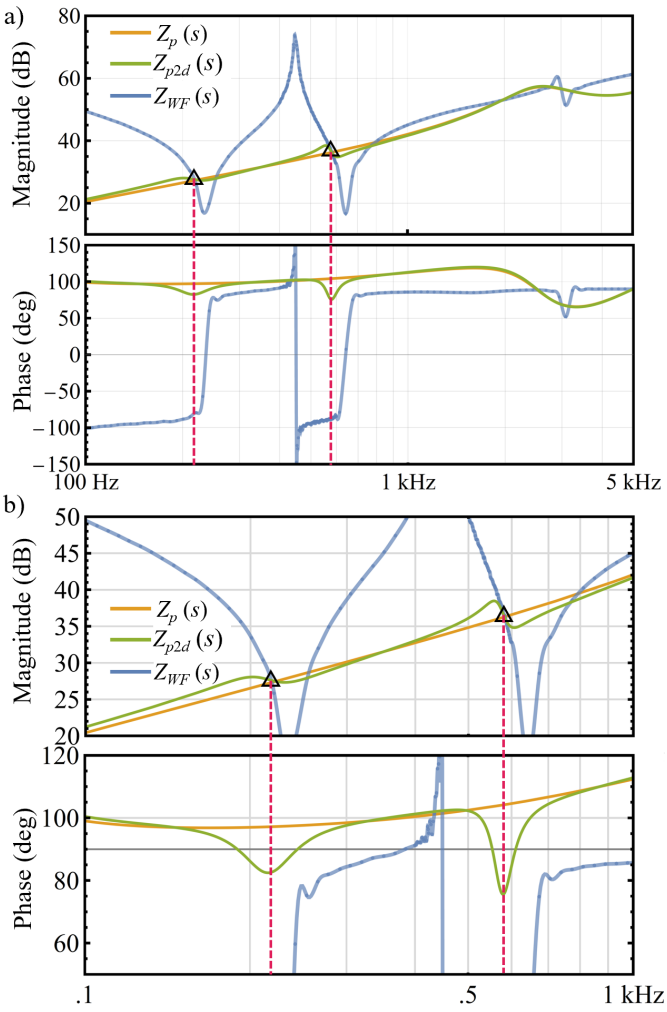

Fig. 21. a) Impedance responses of: undamped and damped AVC-MMC (single-loop fixed V_{ac} & f mode) against Type-IV wind farm; b) zoom-in view of impedance responses plotted in a).

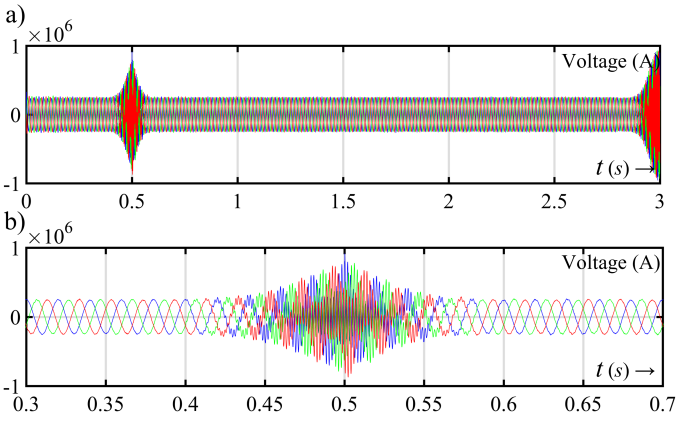

Fig. 22. Simulated time-domain responses: a) overall response of MMC voltage; b) zoom-in view of MMC voltage in 0.3 $\sim$ 0.7s.

VI. CONCLUSION

The paper presented a detailed process to simplify the complete matrix-based impedance model of MMC into a high-frequency impedance model, which is suitable for the design of a damping controller to suppress high-frequency oscillations of MMC. Based on the derived high-frequency impedance model of MMC, this paper discussed the effects and comprehensive design of the proposed multi-tuned damping controller from a virtual admittance perspective, enabling simultaneous damping of MMC impedance around multiple resonance frequencies

in the high-frequency range. By carefully considering and compensating the coupling effect among multiple damping controllers targeting oscillations at different frequencies, potential and unintended interferences are avoided. The performance of the proposed narrowband damping method was verified through EMT simulations, demonstrating its effectiveness in suppressing high-frequency oscillations in three distinct MMC-based applications. This work has laid a solid foundation for further research and development of adaptive damping control schemes for MMCs in various applications.

REFERENCES

[1] C. Buchhagen, C. Rauscher, A. Menze, and J. Jung, "BorWin1 - First experiences with harmonic interactions in converter dominated grids," in *International ETG Congress 2015; Die Energiewende - Blueprints for the new energy age*, pp. 1–7, 2015.

[2] H. Saad, Y. Fillion, S. Deschanvres, Y. Vernay, and S. Dennetière, "On resonances and harmonics in HVDC-MMC station connected to ac grid," *IEEE Transactions on Power Delivery*, vol. 32, pp. 1565–1573, January 2017.

[3] C. Zou and *et al.*, "Analysis of resonance between a VSC-HVDC converter and the ac grid," *IEEE Transactions on Power Electronics*, vol. 33, pp. 10157–10168, February 2018.

[4] Y. Li, T. An, D. Zhang, X. Pei, K. Ji, and G. Tang, "Analysis and suppression control of high frequency resonance for MMC-HVDC system," *IEEE Transactions on Power Delivery*, vol. 36, no. 6, pp. 3867–3881, 2021.

[5] P. Huang and J. Sun, "Mitigation of MMC high-frequency resonance by narrowband damping," in *2021 IEEE 22nd Workshop on Control and Modelling of Power Electronics (COMPEL)*, pp. 1–7, IEEE, 2021.

[6] L. Harnefors, "Proof and application of the positive-net-damping stability criterion," *IEEE Transactions on Power Systems*, vol. 26, pp. 481–482, February 2011.

[7] J. Sun and H. Liu, "Sequence impedance modeling of modular multilevel converters," *IEEE Journal of Emerging and Selected Topics in Power Electronics*, vol. 5, no. 4, pp. 1427–1443, 2017.

[8] B. Zhang, X. Du, C. Du, J. Zhao, and F. Li, "Stability modeling of a three-terminal mmc-hvdc transmission system," *IEEE Transactions on Power Delivery*, vol. 37, no. 3, pp. 1754–1763, 2022.

[9] J. Lyu, X. Zhang, X. Cai, and M. Molinas, "Harmonic state-space based small-signal impedance modeling of a modular multilevel converter with consideration of internal harmonic dynamics," *IEEE Transactions on Power Electronics*, vol. 34, no. 3, pp. 2134–2148, 2019.

[10] J. Lyu, X. Cai, and M. Molinas, "Optimal design of controller parameters for improving the stability of MMC-HVDC for wind farm integration," *IEEE Journal of Emerging and Selected Topics in Power Electronics*, vol. 6, no. 1, pp. 40–53, 2018.

[11] H. Wu, X. Wang, L. Kocewiak, and L. Harnefors, "Ac impedance modeling of modular multilevel converters and two-level voltage-source converters: Similarities and differences," in *2018 IEEE 19th Workshop on Control and Modeling for Power Electronics (COMPEL)*, pp. 1–8, 2018.

[12] H. Wu, X. Wang, Ł. Kocewiak, J. Hjerrild, and M. Kazem, "Passivity-based harmonic stability analysis of an offshore wind farm connected to a mmc-hvdc," in *18th Wind Integration Workshop*, 2019. 18th Wind Integration Workshop ; Conference date: 16-10-2019 Through 18-10-2019.

[13] W. Xu, T. Ding, and B. Liang, "Resonance-free shunt capacitors—configurations, design methods and comparative analysis," *IEEE Transactions on Power Delivery*, vol. 31, pp. 2287–2295, December 2015.

[14] Z. Xu, B. Li, X. Wang, F. Blaabjerg, and D. Xu, "High-frequency resonance suppression based on unified mmc high-frequency impedance model," *IEEE Transactions on Power Electronics*, vol. 37, no. 12, pp. 14755–14769, 2022.

[15] X. Wang, F. Blaabjerg, and P. C. Loh, "Virtual RC damping of *LCL*-filtered voltage source converters with extended selective harmonic compensation," *IEEE Transactions on Power Electronics*, vol. 30, no. 9, pp. 4726–4737, 2015.

[16] Y. Song, F. Blaabjerg, and X. Wang, "Analysis and active damping of multiple high frequency resonances in DFIG system," *IEEE Transactions on Energy Conversion*, vol. 32, no. 1, pp. 369–381, 2017.

[17] W. Cao, Y. Ma, and F. Wang, "Adaptive impedance compensation of inverters for stable grid integration based on online resonance detection," in *2019 IEEE Applied Power Electronics Conference and Exposition (APEC)*, pp. 3151–3158, IEEE, 2019.

[18] E. Guest, T. W. Rasmussen, and K. H. Jensen, "An impedance-based active filter for harmonic damping by type-IV wind turbine," in *proceedings of 17th Wind Integration Workshop (WIW)*, pp. 1–6, Energynautics GmbH, 2018.

[19] E. Guest, K. H. Jensen, and T. W. Rasmussen, "Mitigation of harmonic voltage amplification in offshore wind power plants by wind turbines with embedded active filters," *IEEE Transactions on Sustainable Energy*, vol. 11, no. 2, pp. 785–794, 2020.

[20] X. Wang, Y. W. Li, F. Blaabjerg, and P. C. Loh, "Virtual-impedance-based control for voltage-source and current-source converters," *IEEE Transactions on Power Electronics*, vol. 30, no. 12, pp. 7019–7037, 2015.

[21] P. Huang and L. Vanfretti, "Adaptive passivity compensation of grid-following mmc for stable grid integration," in *2022 IEEE Industry Applications Society Annual Meeting (IAS)*, pp. 1–8, 2022.

[22] L. Chen, X. Xie, M. Song, Y. Li, and Y. Zhang, "Estimation of high-frequency oscillation's magnitude and frequency based on multi-tone fir filter," *IEEE Transactions on Power Systems*, vol. 38, no. 1, pp. 528–536, 2023.

[23] J. Man, L. Chen, V. Terzija, and X. Xie, "Mitigating high-frequency resonance in MMC-HVDC systems using adaptive notch filters," *IEEE Transactions on Power Systems*, pp. 1–1, 2021.

[24] L. Kong, S. Wang, N. Praisuwanna, S. Zhang, L. Qiao, F. Wang, and L. M. Tolbert, "Dc impedance model of mmc considering capacitor voltage and circulating current dynamics," in *2019 IEEE Energy Conversion Congress and Exposition (ECCE)*, pp. 646–653, 2019.

[25] H. Wu, X. Wang, and L. H. Kocewiak, "Impedance-based stability analysis of voltage-controlled mmcs feeding linear ac systems," *IEEE Journal of Emerging and Selected Topics in Power Electronics*, vol. 8, no. 4, pp. 4060–4074, 2020.

[26] Z. Xu, B. Li, L. Han, J. Hu, S. Wang, S. Zhang, and D. Xu, "A complete hss-based impedance model of mmc considering grid impedance coupling," *IEEE Transactions on Power Electronics*, vol. 35, no. 12, pp. 12929–12948, 2020.

[27] U. Karaagac, J. Mahseredjian, L. Cai, and H. Saad, "Offshore wind farm modeling accuracy and efficiency in mmc-based multiterminal hvdc connection," *IEEE Transactions on Power Delivery*, vol. 32, no. 2, pp. 617–627, 2017.

[28] L. Fan and Z. Miao, "Admittance-based stability analysis: Bode plots, nyquist diagrams or eigenvalue analysis?," *IEEE Transactions on Power Systems*, vol. 35, no. 4, pp. 3312–3315, 2020.

[29] L. Harnefors, A. G. Yepes, A. Vidal, and J. Doval-Gandoy, "Passivity-based controller design of grid-connected VSCs for prevention of electrical resonance instability," *IEEE Transactions on Industrial Electronics*, vol. 62, no. 2, pp. 702–710, 2015.

[30] R. G. Lyons, *Understanding Digital Signal Processing*. Pearson Education, 2010.

[31] E. Guest and N. Mijatovic, "Discrete-time complex bandpass filters for three-phase converter systems," *IEEE Transactions on Industrial Electronics*, vol. 66, no. 6, pp. 4650–4660, 2019.

[32] X. Guo, W. Wu, and Z. Chen, "Multiple-complex coefficient-filter-based phase-locked loop and synchronization technique for three-phase grid-interfaced converters in distributed utility networks," *IEEE Transactions on Industrial Electronics*, vol. 58, pp. 1194–1204, April 2011.

[33] A. BERMAN and R. J. PLEMMONS, "Chapter 2 - nonnegative matrices," in *Nonnegative Matrices in the Mathematical Sciences* (A. BERMAN and R. J. PLEMMONS, eds.), pp. 26–62, Academic Press, 1979.

[34] R. S. Varga, *Geršgorin and His Circles*. Springer Berlin, Heidelberg, 2004.

[35] W. S. Meyer and H. W. Dommel, "Numerical modelling of frequency-dependent transmission-line parameters in an electromagnetic transients program," *IEEE Transactions on Power Apparatus and Systems*, vol. PAS-93, no. 5, pp. 1401–1409, 1974.

[36] H. W. Dommel, *Electromagnetic Transients Program Reference Manual (EMTP Theory Book)*. Bonneville Power Administration, 1986.

Pengxiang Huang (S'21) received the B.S. degree from the Shanghai University of Electric Power, Shanghai, China, and the M.S. degree from George Washington University, Washington, DC, USA, all in electrical engineering. He is currently working toward the Ph.D. degree in electrical engineering at Rensselaer Polytechnic Institute, Troy, NY, USA.

His current interests are in renewable energy integration, flexible ac transmission system and MMC-based HVDC systems

Luigi Vanfretti Luigi Vanfretti (Senior Member, IEEE) was born in Guatemala and obtained his Engineering Degree with a concentration in Electrical Power in 2005 from Universidad de San Carlos de Guatemala. He then received the M.Sc. and Ph.D. degrees in electric power engineering from the Rensselaer Polytechnic Institute (RPI), Troy, NY, USA, in 2007 and 2009, respectively. He held postdoctoral research posts both at RPI and KTH Royal Institute of Technology, Sweden, in 2010.

He is currently a Full Professor at Rensselaer Polytechnic Institute, since July 2022, where he was a tenured Associate Professor from 2017-6/2022-6. At RPI, he leads research projects in his laboratory and with his research team, ALSETLab, in the domains of electrical power systems and aircraft electrification.